Role of anion on the electrochemical performance of MnCo chalcogenides

DOI: 10.1016/j.est.2023.108718
Handle: http://hdl.handle.net/1942/41715

Role of anion on the electrochemical performance of MnCo chalcogenides

Ying Zhang [a], Weikang He [a], Jingjing Li [a], Yuanyuan Zhang [a], Juan Yang [a], Ting Zeng [a]*, Nianjun Yang [b]

[a] School of Chemistry and Environmental Engineering, Key Laboratory of Green Chemical Engineering Process of Ministry of Education, Hubei Key Laboratory of Novel Reactor and Green Chemical Technology, Wuhan Institute of Technology, Wuhan 430073, China

[b] Department of Chemistry, Hasselt University, Agoralaan 1 - Buidling D, 3590 Diepenbeek, Belgium

Corresponding author. E-mail address: tingzeng1201@wit.edu.cn

ABSTRACT: Transition metal chalcogenides (TMCs) own multiple oxidation states and enhanced electroactivities of metal centers. To reveal the influence of anions in TMCs on the electrochemical performance of these promising supercapacitor electrode materials, three manganese and cobalt chalcogenides, namely MCS, MCSe, and MCTe are synthesized and characterized. In alkaline electrolytes, the capacities at a current density of 1 A g^{-1} are 920.5, 529.9, and 131.3 C g^{-1}, respectively. MCS exhibits a superior specific capacity, enhanced rate capability, and long-term cycling stability. Consequently, anions of S, Se and Te determine electrochemical performance of TMCs. An ensembled quasi-solid asymmetric supercapacitor, consisting of the MCS cathode and an anode of a holey reduced graphene oxide (hrGO) coupled with 2,2,6,6-Tetramethylpiperidin-1-oxyl (TEMPO) possesses a maximum energy density of 43.7 Wh kg^{-1} at a power density of 750.3 W kg^{-1} or a maximum power density of 14898.6 W kg^{-1} at an energy density of 15.3 Wh kg^{-1}. It retains 98.3% of initial capacity even after 7500 charge/discharge cycles at a current density of 10 A g^{-1}. This study provides insight into the synthesis and utilization of TMCs for the ensemble of high-performance supercapacitors.

Keywords: transition metal chalcogenides, asymmetric supercapacitors, energy density, electrode kinetics

1. Introduction

Global warming is becoming increasingly severe and ecological balance is seriously out of balance [1]. The use of alternative renewable energy sources (e.g., solar, hydropower, wind, and tidal energy) to replace limited fossil fuels and coals is thus of great significance [2-4]. In this regard, various kinds of energy storage devices are designed and developed to transfer and store the electricity generated from these renewable sources. Supercapacitor (SC) is one typical electrochemical energy storage system. High-performance SCs are expected to provide high power densities like traditional capacitors as well as high energy densities like traditional batteries [5-8]. Compared with batteries, SCs have the advantages of high-power densities, faster charging rates, and long cycling life. For SCs, three kinds of mechanisms have been employed to store electrical energy, namely based on electrical double-layer capacitance, pseudocapacitance and battery-type. Up to date, SCs are still hard to replace batteries in most practical applications due to their low specific energies, linear discharge voltages, and relatively high costs [9]. Therefore, new electrodes, membranes (separators) inserted between two electrodes, and the electrolytes need to further designed, synthesized, and developed.

The used electrodes and electrolytes are known to mainly determine the SC performance. Transition metal compounds have been frequently utilized to ensemble the SCs. Transition metal chalcogenides (TMCs), commonly referring to transition metal sulphides, transition metal selenides, and transition metal tellurides are extremely attractive since TMCs possess variable band gaps, distinct stoichiometry, tuneable structures and material diversity [10-12]. Compared to the corresponding transition metal oxides, TMCs have shown higher capacity since they have higher electronic conductivities and more channels for ion transport. The reason behind is the weaker M–S (Se or Te) bonds in comparison to the M–O bonds [13]. In this context, sulphides and selenides of manganese, cobalt, nickel, molybdenum, tin, and tungsten have been utilized as the electrode materials to ensemble SCs [14-17]. Among them, cobalt and nickel tellurides are two typical SC materials [18]. Note that mixed TMCs and hybrid TMCs own unique features over these TMCs with one single metal centres and therefore have been applied as the battery-type electrode materials. Owing to complementation and synergy, increased conductivity and enhanced redox reactions, efficient variable valence states, these TMCs with double or triple metal centres exhibit superior electrochemical performance to those only with one metal centre. Of special interests, these materials have been widely investigated, including $ZnCo_2O_4$, $NiFe_2O_4$, $NiCo_2O_4$, $NiCo_2S_4$, $MnCo_2S_4$, $NiCo_2S_4$,

$NiCo_2S_4$, $CuCo_2S_4$[19-22]. Meanwhile, there are mixed transition metal oxides or chalcogenides, which exhibit controllable structures, relatively low-costs, and excellent dielectric properties. It has to highlight here that the conductivity and permittivity of TMCs are significantly influenced by anions inside TMCs. Surprisingly, the effect of anions inside TMCs on their electrochemical performance has been not well understood and reported up to date.

In this work, we synthesized MCS, MCSe, and MCTe materials (denoted as $MnCo_2S_4$, $MnCo_2Se_4$, and $MnCo_2Te_4$, respectively) on a nickel foam. The choice of a Ni foam as a conductive scaffold during the synthesis processes of these TMC materials originates from its three-dimensional (3D) and interconnected stems, its porous surface, and its high electrical conductivity. A Na_2S solution [23], a SeO_2 solution [23], and a Na_2TeO_3 solution [24] were applied for the sulfidation, selenidation, and telluridation processes on the MnCo-LDH precursor that was the *in-situ* deposited on the porous Ni foam during a hydrothermal reaction. During these anion-exchange processes, phase transformation from the precursor to MCS, MCSe, and MCTe nanorods was realized. The structures and morphologies of three TMCs were then characterized using different microscopy, spectroscopy, and electrochemical techniques. Importantly, the electrochemical performance of three TMCs were investigated and compared by means of cyclic voltammetry (CV), the galvanostatic charge-discharge method (GCD), and electrochemical impedance spectroscopy (EIS). The effect of anions inside TMCs on their electrochemical performance, which has been seldom reported and clarified. By use of the best MCS as the cathode and a holey reduced graphene oxide (hrGO) matched with redox electrolyte as the anode, an asymmetric supercapacitor was ensembled. Its performance (e.g., capacity, capacity retention, power density, and energy density) was examined together with its potential and practical applications.

2. Experimental

2.1. Materials

All the chemicals were analytical grade and used as received without any further purification. A nickel foam substrate was cut into pieces with a size of 2.0 × 4.0 cm^2. To remove oxides, impurities, and organic pollutants on the surface of the nickel foam, the cut pieces were washed with deionized water, 5 wt% hydrochloric acid, ethanol, and deionized water. The cleaned pieces were then dried in the oven at 60 °C for 7 h.

A MnCo-LDH precursor (denoted as MC-LDH) was prepared on the nickel foam through a hydrothermal method [25]. In the first step, 1 mM $Mn(NO_3)_2$, 2 mM $Co(NO_3)_2$, 3 mM NH_4F, and 6 mM $CO(NH_2)_2$ aqueous solutions were mixed and stirred at least for 30 min till a uniform and stable

pink solution was obtained. In the second step, a precleaned nickel foam was soaked in the pink solution (70 mL) for 10 min. Subsequently, the mixed solution and nickel foam were transferred to a 50 mL stainless steel Teflon lined autoclave and hydrothermally treated at 180 °C for 8 h. After being naturally cooled, the obtained nickel foam was cleaned several times in an ultrasonic bath till the surface suspended materials were fully removed. After copiously rinsing this nickel foam with water and ethanol, it was dried at 70 °C for overnight. The specific mass of as-obtained MnCo product was about 1.7 mg cm^{-2}.

The MC-LDH precursor was further hydrothermally treated with respective chalcogenide precursors to prepare MCS, MCSe, and MCTe materials. For example, to prepare MCS from the MC-LDH precursor, a sulfidation process was applied [23]. Briefly, the precursor was firstly immersed into 40 mL water containing 0.3 g $Na_2S{\cdot}9H_2O$ for 10 min. The solution was then transferred to a 50 mL Teflon-lined stainless-steel autoclave and kept at 160 °C for 8 h. To remove loose particles, the MCS deposited on the nickel foam was cleaned with water and ethanol for 3 times and further dried at 70 °C for overnight. The weight of MCS that was attached to the nickel foam was about 2.5 mg cm^{-2}. Similar steps were followed to synthesize MCSe [23] and MCTe [24], where 0.055 g SeO_2 and 0.111 g Na_2TeO_3 were used, respectively. The mass loadings of MCSe and MCTe were about 4.0 and 6.8 mg cm^{-2}, respectively.

2.2. Materials characterization

A field-enhanced scanning electron microscope (Germini SEM 300 microscope, Zeiss, German) was employed to record scanning electron microscopy (SEM) images of as-synthesized materials. Transmission electron microscopy (TEM), high resolution TEM (HRTEM) and selected area electron diffraction (SAED) pattern images of as-synthesized materials were collected on a JREOL-JEM-2100 (JEOL, Japan) instrument. X-ray photoelectron spectroscopy (XPS) was conducted on an AXIS-ULTRA DLD-600W (Shimadzu-Kratos Company, Japan). X-ray diffraction (XRD) patterns were collected on a Bruker D8 equipped with a DaVinci design instrument.

2.3. Electrochemical measurements

All electrochemical tests were carried out on a VSP-300 multi-channel electrochemical workstation (Bio-Logic Science Instruments, France). The electrochemical properties of the electrodes were investigated by means of CV, GCD and EIS methods. In a typical three-electrode electrochemical system, a graphite paper counter electrode and a Hg/HgO reference electrode were

used. To investigate the electrochemical performance of TMC materials, the used electrolyte was 6 M KOH aqueous solution. To check the electrochemical performance of the hrGO electrode, a solution of 10 mM 2,2,6,6-Tetramethylpiperidin-1-oxyl (TEMPO) dissolved in 2 M KOH was applied as the electrolyte.

In a two-electrode system or an assembled asymmetric supercapacitor device, the negative electrode was the hrGO-coated nickel foam and the positive electrode was the MCS coated Ni foam. They were assembled with a piece of Nafion-117 membrane as the separator. The hrGO electrode was matched with the gel anolyte of KOH + TEMPO, while a MCS electrode was matched with the KOH/PVA gel catholyte.

In order to calculate the mass capacity (C, C g^{-1}), energy density (E, Wh kg^{-1}), and power density (P, W kg^{-1}) of the assembled ASC device, the following equations were used [26, 27]:

$$C = \frac{S}{2\,v \times m} \quad (1)$$

$$C = \frac{I \times \Delta t}{m} \quad (2)$$

$$E = \frac{1}{7.2} \times C \times \Delta V \quad (3)$$

$$P = \frac{E \times 3600}{\Delta t} \quad (4)$$

$$Q_+ = Q_- \quad (5)$$

$$\frac{m_+}{m_-} = \frac{C_-}{C_+} \quad (6)$$

where S is the charge (or area) enclosed in a CV within the scanned potential window (ΔV), v is the scan rate (V s^{-1}), m represents the loading mass (g) of an active material, I represents the current density (A g^{-1}), and Δt is the discharge time (s). For Equation (5) and (6), "+" and "–" represent the positive and negative electrodes, respectively. The terms Q_+ and Q_- refer to the charges transferred on the positive and negative electrodes, respectively. In the assembly of this ASC device, the mass ratio between the positive (m_+) electrode and negative (m_-) one was fixed to be approximately 0.8, and the scan rate was set to 20 mV s^{-1}.

3. Results and discussion

3.1. Materials characterization

The synthesis process of these TMC materials (namely MCS, MCSe, and MCTe) is schematically illustrated in **Fig. S1**. In the process of hydrothermal synthesis, manganese and cobalt ions are converted into the MnCo precursor (MC-LDH) under alkaline conditions. The surface morphologies and microstructures of the MnCo precursor was characterized. From the SEM image of the MC-LDH at a low magnification (**Fig. S2A**), one can clearly tell that it is needle-like. These nanoneedles are uniformly and densely distributed onto the surface of the nickel foam. Their growth directions are predominantly vertical and slightly inclined. The roots of these nanoneedles are thicker while their tips are thinner. In the SEM image of the MnCo precursor at a high magnification (**Fig. S2B**), the MC-LDH nanoneedles are found to have a smooth exterior. An average diameter of the MC-LDH nanoneedles was estimated to be between 80 and 100 nm. These nanoneedles maintain a relatively large gap between each other. Such gaps are important since they are expected to facilitate the subsequent sulfidation, selenation, and tellurization processes. It is known that the anion-exchange reaction of the MC-LDH precursor takes place under a hydrothermal environment. The added X^{2-} (X= S, Se, Te) anions corrode the precursor from its outer (e.g., surface) to the inter, leading to the formation of the MnCo chalcogenides [23, 24, 26]. Driven by the Kirkendall effect, simultaneous involvement of the inward diffusion of different X^{2-} anions and the outward diffusion of different metal cations are expected. The final structures and compositions of three TMCs are thereby different and possible to be tuned.

Subsequently, the surface morphologies and microstructures of MCS, MCSe, and MCTe were examined characterized by means of SEM **(Fig. 1A-F)** and TEM **(Fig. 1G-I)**. The MCS material retains a similar needle morphology as the MC-LDH (**Fig. 1A)**. These MCS nanoneedles are dense and uniform. These interlaced nanoneedles are grown. Their surface is rough and slightly concave. Their diameters are around 80-150 nm **(Fig. 1D)**. For the MCSe material, it is more like corncobs **(Fig. 1B)**. The alignment of these hollow nanotube arrays on the nickel foam are clearly visible. There are even some hollow nanotubes with opening ends **(Fig. 1E)**. Similarly, the MCTe material consists of hollow nanotubes with a rough surface nature **(Fig. 1C, F)**. The TEM images of MC-LDH and three TMC materials provide further information about the morphologies and structures of these materials. The structures in these TEM images are analogous to those shown in the related SEM images. The MC-LDH precursor has a needle-like structure with a very smooth surface. Its average diameter is approximately 100 nm **(Fig. S2C)**. The MCS material has a nanowire-like structure, and

the average diameter of these nanowires is about 120 nm **(Fig. 1G)**. Clearly, the MCSe **(Fig. 1H)** and MCTe **(Fig. 1I)** materials exist in the form of hollow nanotubes, whose diameters are approximately 100-120 nm. Both own a wrinkled structure on their surface. The inner hollow tubular nanostructure of the MCSe material has a shell thickness of about 35 nm, while that of the MCTe material is about 20 nm. The element mapping of the TMCs (**Fig. S3)** was also conducted by energy-dispersive X-ray spectroscopy (EDS). It is clear that the elements of Mn and Co distribute on all samples, while the elements of S, Se, and Te are clearly visible at the mapping images of the MCS, MCSe, and MCTe, respectively. The results suggest that three different TMCs materials have been synthesized. For the precursor, MCS, MCSe, and MCTe, they feature their three-dimensional (3D) structures. Namely, they have large surface areas and many available channels for electrochemical processes. Consequently, they are expected to feature high performance for electrochemical energy storage.

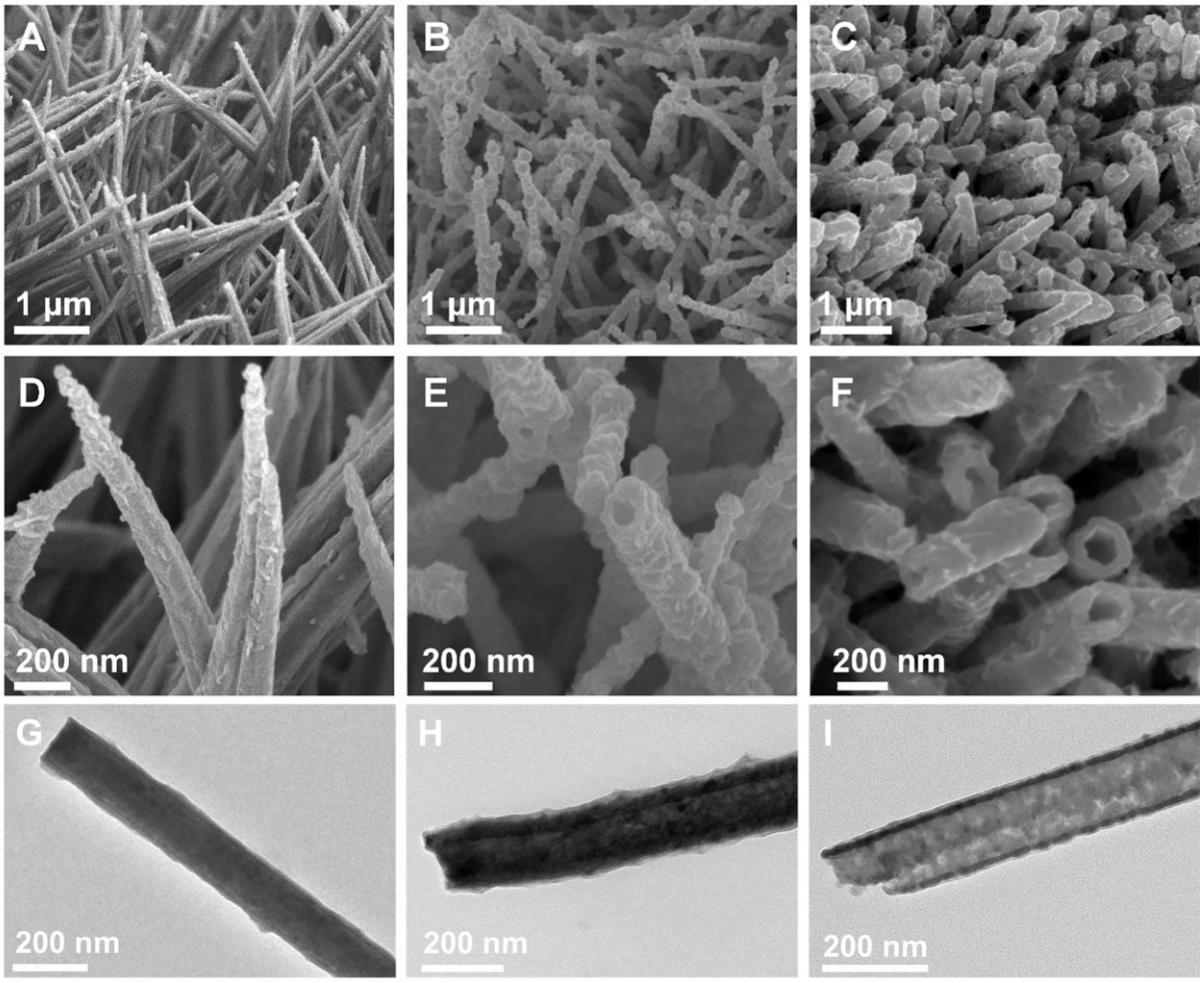

Fig. 1. (A-F) SEM images of MCS (A, D), MCSe (B, E), and MCTe (C, F) at different magnifications; (G-I) TEM images of MCS (G), MCSe (H), and MCTe (I).

The X-ray diffraction (XRD) characterization of the MC-LDH precursor, MCS, MCSe, and MCTe was further conducted. In the XRD patterns of the MnCo precursor **(Fig. S4A)**, the diffraction peaks at 10.0°, 33.3°, 34.8°, 39.1° and 59.1° are from the (003), (009), (012), (015) and (110) planes of a typical layered double hydroxide (LDH) phase [28], respectively. Three additional and sharp diffraction peaks at 44.6°, 51.9° and 76.3° can be assigned to the nickel foam substrate (JCPDS No. 1-1266) [29], as indicated as "Ni" in the plot. Although there are no standard International Centre for Diffraction Data (ICD) patterns for bimetallic MnCo chalcogenides, their diffraction peaks are similar to the cubic Co_3S_4 (JCPDS No. 47-1738), CoSe (JCPD No. 70-2870), and CoTe (JCPDS No. 34-0420) which were utilized as the bases for the analysis of the crystalline structures of MCS, MCSe, MCTe. In their XRD patterns (**Fig. 2A**), the diffraction peaks of MCS appear at 31.2°, 37.9°, 50.0°, and 55.3°. They are in line with (311), (400), (511), (440) planes of cubic Co_3S_4 (JCPDS No. 47-1738) [30, 31], respectively. For MCSe, its XRD diffraction peaks are located at 32.9°, 50.0°, 61.6° and 70.0°, corresponding to the (101), (110), (210), (202) planes of the CoSe, (JCPDS No 70-2870) [32, 33], respectively. Similarly, the XRD spectrum of MCTe exhibits the characteristic diffraction peaks at 31.6°, 42.9°, 47.1° and 58.3°, resulting from (101), (102), (110) and (112) planes of CoTe (JCPDS No. 34-0420) [34, 35], respectively. In **Fig. 2H, J** and **L**, the high-resolution TEM (HRTEM) images of these composite exhibits highly resolved lattice fringes with different lattice spacings, corresponding to the different planes. As well as the selected area electron diffraction (SAED) patterns (**Fig. 2I, K** and **M**), which illustrate a set of concentric diffraction rings associated with the respective lattices [36, 37]. According to these results, the nanostructure is consistent with the XRD analysis.

The XPS spectra of three TMC materials were also recorded. Their XPS survey spectra confirm the existence of different elements in these bimetallic chalcogenides **(Fig. S4B)**. In both Mn 2p and Co 2p XPS spectra, two spin-orbit doublets are identified, owing to the divalent (Mn^{2+}, Co^{2+}) and trivalent (Mn^{3+}, Co^{3+}) states. The high-resolution XPS spectrum of the Mn 2p region **(Fig. 2B)** reveals spin–orbit splitting into two peaks at binding energies of 641.5 and 653.5 eV, which can be assigned to Mn $2p_{1/2}$ and Mn $2p_{3/2}$ [38, 39], respectively. Other two peaks located at 641.2 eV and 647 eV are ascribed to the signal of Mn^{3+} and Mn^{3+} species. The spin-orbit energy splitting of the core level of Mn $2p_{3/2}$ and Mn $2p_{1/2}$ for MCS, MCSe, and MCTe are 12.6, 12.0, and 11.9 eV, respectively. In their Co 2p spectra **(Fig. 2C)**, two spin/orbit bimodal peaks are visible along with two satellite peaks that are associated with shake-up. In the Co 2p XPS spectrum of MCS, where the two deconvoluted peaks at 781.6 and 797.1 eV are attributed to the Co^{2+} species, while the other two deconvoluted peaks at 778.6 and 792.9 eV are attributed to Co^{3+}. For MCSe, its Co 2p XPS peaks at 781.2 and 796.8 eV are assigned to the Co^{2+} species, while those at 778.5 and 792.8 eV are attributed to the Co^{3+} species. The

peaks appeared at 777.4/792.5 and 780.6/796.3 eV in the Co 2p XPS spectrum of MCTe indicate the existence of the Co^{2+} and Co^{3+} species, respectively. Meanwhile, two shape-up satellite peaks are presented at around 802.0 and 785.5 eV in the XPS spectra of three TMC materials. Based on the different induction effects caused by the reduced electronegativity of S, Se, Te, the peaks of Co 2p shifted to the lower field due to the different induction effects, and the calculated spin orbital energy separation was changed from 15.4 eV to 15.7 eV, which indicated the existence of Co^{2+}/Co^{3+} and confirmed the chemical interaction between Co and these elements [40].

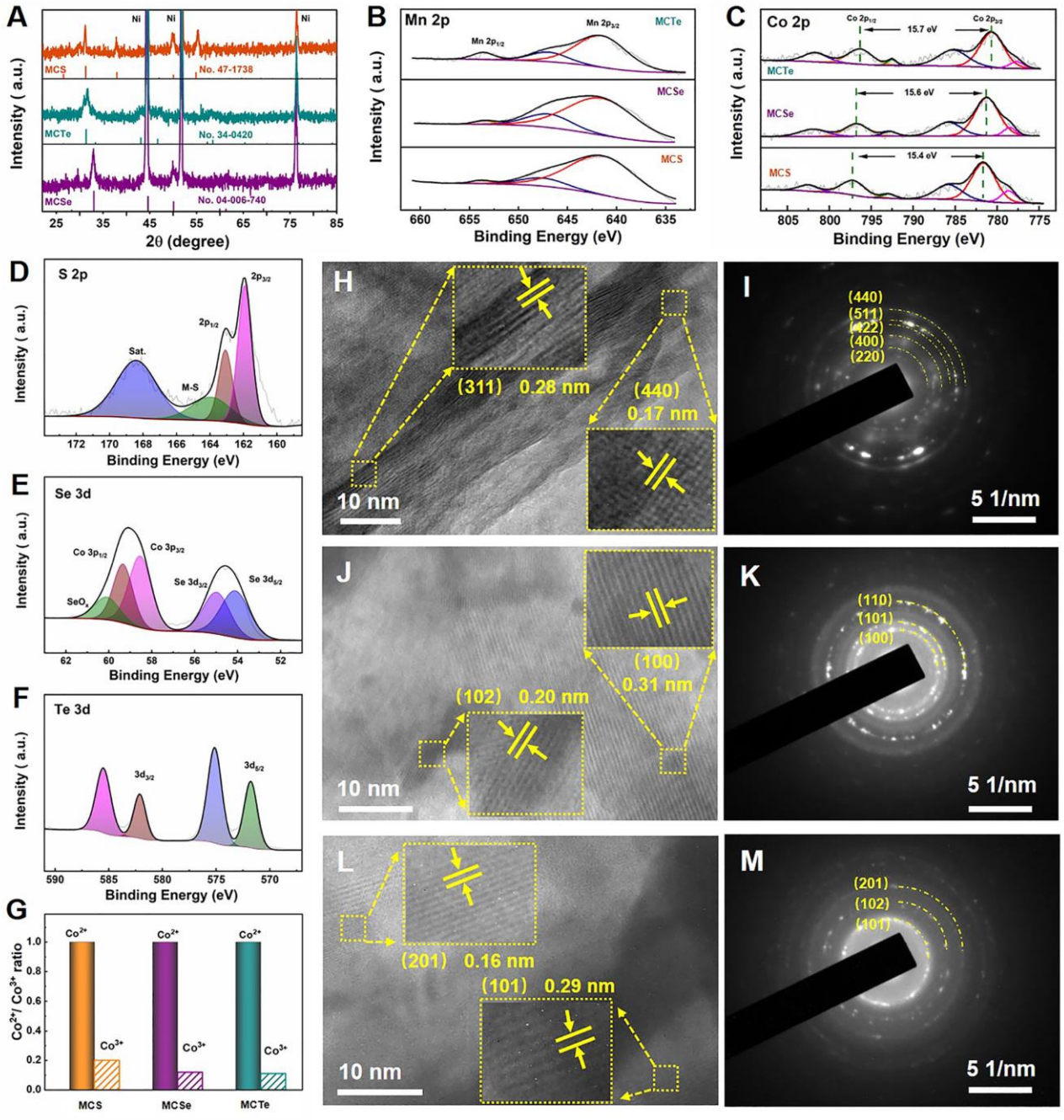

Fig. 2. (A) XRD patterns of MCS, MCSe, and MCTe; XPS of Mn 2p (B) and Co 2p (C) spectra of MCS, MCSe, and MCTe; (D) XPS S 2p spectrum of MCS, (E) XPS Se 3d spectrum of MCSe; (F)

XPS Te 3d spectrum of MCTe. (G) the content ratios of Co^{2+}/Co^{3+} in MCS, MCSe, and MCTe. HRTEM and SAED images of MCS (H, I), MCSe (J, K), and MCTe (L, M).

Moreover, the S 2p peak for MCS can be divided into three peaks along with a satellite peak **(Fig. 2D)**. These peaks located at 161.9 and 163.1 eV are related with the S $2p_{3/2}$ and S $2p_{1/2}$, respectively. Other two peak appeared at 163.9 and 168.4 eV are ascribed to the metal-sulphate bond and the satellite peak[24, 36].In the XPS Se 3d spectrum of the MCSe material (**Fig. 2E**), the peaks located at 54.9 and 54.1 eV correspond to Se $3d_{3/2}$ and Se $3d_{5/2}$, respectively. They confirm the presence of a Se^{2-} valence. The Se–O peak at 60.1 eV is probably due to the oxidized selenium or selenium oxide. The peak at 58.9 eV evidences that the existence of a Co–Se bond inside MCSe [41]. In the XPS Te 3d spectrum of MCTe (**Fig. 2F**), the peaks at 571.8nd 582.1 eV correspond to the Te $3d_{5/2}$ and Te $3d_{3/2}$ of the Metal-Te bonds [42]. The peaks at 582.1 and 585.5 eV are obviously from the of the Te^{4+} species since tellurides are easily oxidized in the air [43].

Since the energy gap between the main peak of Co 2p and Mn 2p is generally accepted as a parameter to determine the oxidation state of the Co species, the relationship of the contents of Co valence state in MCS, MCSe and MCTe were then estimated *via* refined fitting and quantitative calculations from their XPS Co 2p spectra (**Fig. 2G**). The ratios of Co^{2+}/Co^{3+} are different for three TMC materials. Among them, MCS has the highest ratio, probably resulting in more faradaic reactions at the electrode surface. It has to highlight that these bimetallic chalcogenides own a variety of metal valence states that can facilitate the generation of more active redox sites and therefore increase the diffusion rates of charges and thus their electronic conductivities are expected to be improved. In short, MCS, MCSe, and MCTe are expected to feature improved capacitive performance than those TMCs with individual metal centers.

3.2. Electrochemical performance

The electrochemical performance of the MC-LDH, MCS, MCSe, and MCTe in 6 M KOH aqueous solution was studied using cyclic voltammetry and the GCD technique. In their cyclic voltammograms (CVs) recorded within a potential range of 0 – 0.5 V and at a scan rate of 5 mV s^{-1}, a pair of redox peaks is observed (**Fig. 3A**). They are related with the faradaic processes of the reversible transformation of multivalent Mn and Co species. It is obvious that the CV of MCS owns a higher redox peak intensity and a bigger integrated area. The MCS thus has a larger capacity than

other three counterparts. The redox waves for the MnCo precursor are assumed from the following reactions between Mn and Co cations [25]:

$$Co(OH)_2 + OH^- \leftrightarrow CoOOH + H_2O + e^- \quad (7)$$

$$CoOOH + OH^- \leftrightarrow CoO_2 + H_2O + e^- \quad (8)$$

$$Mn(OH)_2 + OH^- \leftrightarrow MnOOH + H_2O + e^- \quad (9)$$

$$MnOOH + OH^- \leftrightarrow MnO_2 + H_2O + e^- \quad (10)$$

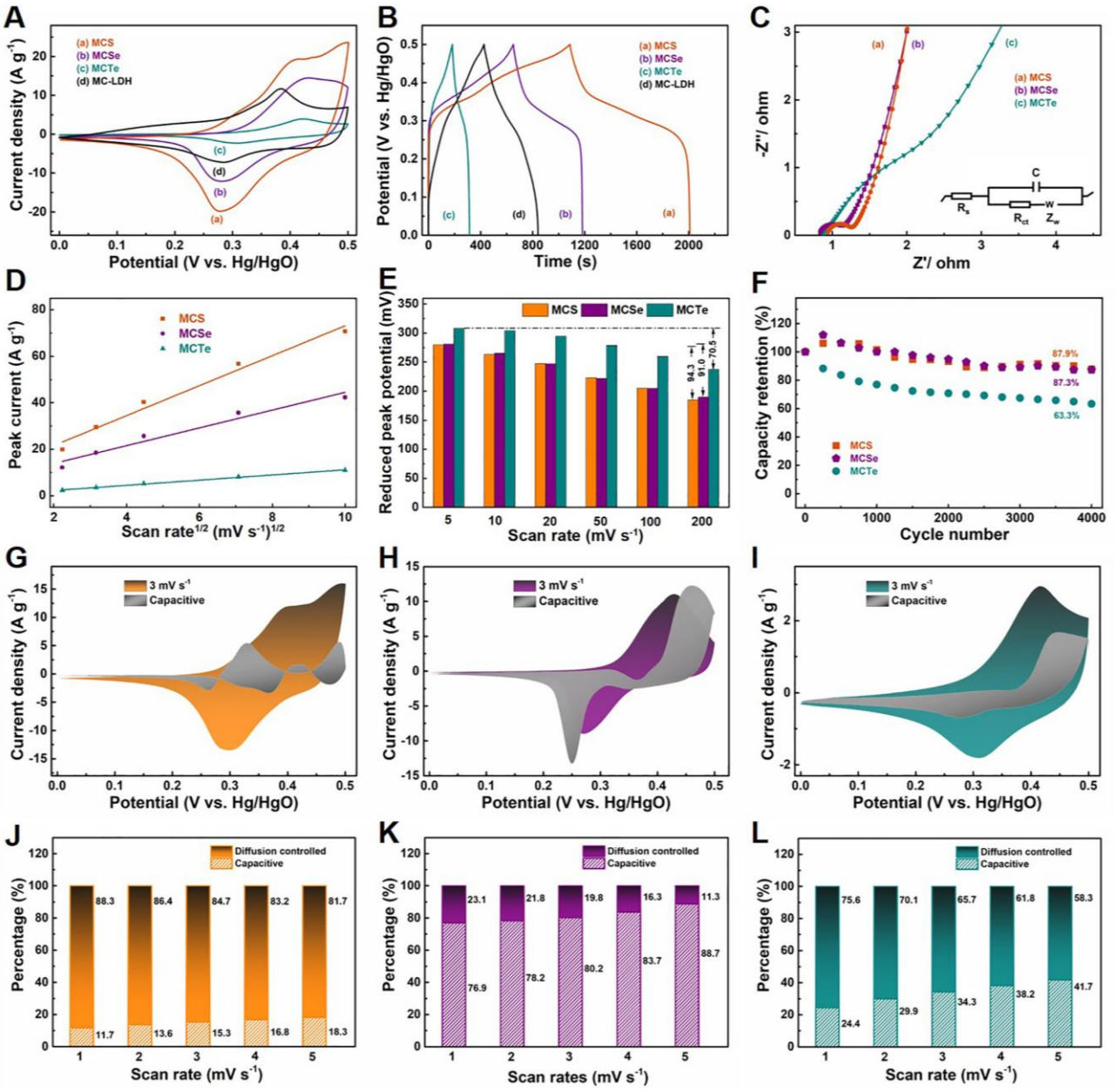

Fig. 3. Capacitive performance of the MC-LDH, MCS, MCSe, and MCTe: (A) CVs; (B) GCD curves; (C) the Nyquist plots; (D) Variation of peak currents as a function of the square roots of scan rates; (E) Variation of the difference between anodic and cathodic peak potentials in the CVs as a function of scan rates; (F) Cycling stability at a constant current density of 10 A g^{-1}; (G-I) The capacitive

contribution of MCS (G), MCSe (H), and MCTe (I) to their charge storage at a scan rate of 3 mV s^{-1}; (J-L) The percentage of capacitive contribution of MCS (J), MCSe (K), and MCTe (L) at different scan rates.

While the redox waves for MCS, MCSe, and MCTe are supposed to be from the reversible faradaic redox processes of $Mn^{2+/3+}$, $Co^{2+/3+}$ and X^{2-} (X = S, Se, Te) in the form of [44-46]:

$$MnCo_2X_4 + 2OH^- + H_2O \leftrightarrow MnXOH + 2CoXOH + 2e^- \quad (11)$$

$$CoXOH + OH^- \leftrightarrow CoXO + H_2O + e^- \quad (12)$$

$$CoX + OH^- \leftrightarrow CoXOH + e^- \quad (13)$$

$$MnX + OH^- \leftrightarrow MnXOH + e^- \quad (14)$$

To reveal electrode kinetics, the CVs of the MC-LDH (**Fig. S5A**), MCS (**Fig. S5B**), MCSe (**Fig. S5C**), and MCTe (**Fig. S5D**) were recorded in 6 M KOH aqueous solution at different scan rates (e.g., from 5 to 200 mV s^{-1}). An increase of scan rate leads to the positive and negative shift of the anodic and cathodic peak potentials, respectively. It is noteworthy that the reduction peaks retain their typical characteristics without obvious distortion, even at high scan rates; while the oxidation peaks fall out of the scanned potential range when the scan rate is too high. In this regard, as-estimated specific capacity is decreased with an increase of scan rate. In our experiments, lower scan rates were applied to get higher specific capacities. The specific capacity of the MnCo precursor, MCS, MCSe, and MCTe that were calculated from their CVs at a scan rate of 5 mV s^{-1} are 392.1, 722.1, 406.2, and 92.3 C g^{-1}, respectively.

The GCD curves of the MC-LDH, MCS, MCSe, and MCTe were further recorded in 6 M KOH aqueous solution at a current density of 1 A g^{-1} (**Fig. 3B**). These GCD curves are nonlinear, where two voltage plateaus are seen during the charge-discharge processes. These results are in accordance with those shown in their CVs, indicating the involvement of faradaic processes. Namely, the MC-LDH, MCS, MCSe, and MCTe have the features of battery-type materials. The MCS possesses a longer discharge time and a bigger specific capacity than the MC-LDH, MCSe, and MCTe, in agreement with the tendency of their specific capacity obtained from those CVs. The GCD curves of the MC-LDH (**Fig. S6A**), MCS (**Fig. S6B**), MCSe (**Fig. S6C**), and MCTe (**Fig. S6D**) were further recorded in 6 M KOH aqueous solution at different current densities (e.g., from 1 to 20 A g^{-1}). At low current densities, they take longer time to finish charge and discharge processes. To compare their specific capacity, the values of the MC-LDH, MCS, MCSe, and MCTe were calculated and

compared (**Fig. S7**) at different current densities. The calculated specific capacity of MCS at a current density of 1 A g^{-1} is 920.5 C g^{-1}, which is superior to that of MCSe (529.9 C g^{-1}), the MC-LDH (415.1 C g^{-1}), and MCTe (131.3 C g^{-1}). At a current density of 20 A g^{-1}, their specific capacities are 489.3, 280.9, 234.0, and 36.8 C g^{-1}, respectively. The corresponding capacitive retentions of the MC-LDH, MCS, MCSe, and MCTe are 56.4%, 53.2%, 53.0% and 28.0%, respectively. Calculated from the CVs and GCD curves of the MnCo precursor, MCS, MCSe, and MCTe, the trend in their specific capacities follows the order of MCS > MCSe > MC-LDH> MCTe. Some comparison of the electrochemical performance of MCS-based electrodes reported in the literature are summarized in **Table S1**.

The Nyquist plots of MCS, MCSe, and MCTe were also recorded (**Fig. 3C**). According to the equivalent circuit model, R_s means the series resistance, C represents the double layer capacitance, R_{ct} is the interfacial charge transfer resistance and W represents the Warburg impedance. The Warburg resistance (Z_w) signifies the diffusion of cations through the electrode materials. Their R_{ct} values follow the order of MCS < MCSe < MCTe. Therefore, MCS has the highest specific capacity and the best rate performance. This is because the atomic weight of tellurium is approximately four times bigger than that of sulfur. Moreover, tellurium is easier to be oxidized than S and Se during the galvanostatic charge/discharge processes. Consequently, anions in the TMCs determine their capacities.

The variation of peak current as a function of square roots of scan rates was further analyzed. For all three TMCs, nearly linear relationship exists (**Fig. 3D**). For MCS, it exhibits the highest slope, indicating a highest electrochemical activity and increased migration ability of hydroxide ion among these TMCs [38]. The difference of anodic and cathodic peak potentials was plotted as a function of scan rate (**Fig. 3E**) in the range of 5 to 200 mV s^{-1}. The reduction peak potential of MCS shifts to the most negative value (94.3 mV). For MCSe and MCTe, their reduction peak potentials shift to 91.0 and 70.5 mV, respectively. The smaller is the shift in peak potential, the less polarization there is in the electrode material during the charge/discharge process. During the rapid Faraday reaction on the surface, the OH^- in the electrolyte cannot diffuse to the surface in time, giving rise to greater polarization. The ion transfer rate of OH^- ions is thus the fastest and the polarization degree of MCS is the highest during its charge/discharge process. In other words, the Faraday reaction of MCS is the fastest, leading to its largest specific capacity. In comparison with MCSe and MCTe, MCS exhibits faster ion migration and redox reaction in an alkaline medium, as well as better energy storage capacity. It again confirms the anion-determined capacities of TMCs.

Furthermore, the cycling performance of MCS, MCSe, and MCTe was examined using the GCD analysis at a current density of 10 Ag^{-1} (**Fig. 3F**). Even after 4000 charge/discharge cycles, MCS

retains 87.9% of its initial capacity, which is higher than that of MCSe (87.3%), and MCTe (63.3%). The excellent stability of MCS was also proved by tiny variation of its Nyquist plots before and after such a cycling test (**Fig. S8**). According to the SEM images (**Fig. S9A-C**), the morphology of three TMCs have undergone some interesting changes after the cyclic stability test. While the surface of MCS still retains the nanoneedles structure, there are some sheet-like morphologies apparent. MCSe exhibits morphological changes due to the adhesion of long tubular structures, resulting in cauliflower-like structures. There are agglomerated nanospherical structures growing on top of the MCTe nanotubes. There is a possibility that the changed morphology is caused by the partial expansion and collapse of the nanostructures over an extended period of charge/discharge. In short, MCS has excellent stability, due to its small volume expansion during the charge/ discharge processes. The weak cycling stability of MCTe is probably due to its readiness to be oxidized during charge/ discharge processes.

It is known that the capacitive contribution to the total charge can be analysed from related CVs. The relationship between the peak current and the sweep rate is described as following [47]:

$$i = av^b \quad (15)$$

$$\log i = b\log v + \log a \quad (16)$$

In generally, *b*-value of 0.5 indicates that the redox reaction is a diffusion-controlled process, whereas *b*-value of 1.0 implies a capacitive process. The calculated *b*-values of MCS, MCSe, and MCTe (**Fig. S10**) are 0.68, 0.79 and 0.64, respectively. Therefore, a hybrid charge storage mechanism exists for three TMCs, consisting of diffusion- and surface capacitive-controlled processes. Based on the calculated *b* value, the energy storage mechanism of MCSe is mainly governed by its capacitive performance. The capacitive contribution is then quantitively determined by use of the equations [47, 48]:

$$i = k_1 v + k_2 v^{1/2} \quad (17)$$

$$i/v^{1/2} = k_1 v^{1/2} + k_2 \quad (18)$$

where the terms of $k_1 v$ and $k_2 v^{1/2}$ represent the capacitive and diffusion-controlled contributions, respectively. For example, the diffusion contribution of MCS is 84.7 % (**Fig. 3G**) at a scan rate of 3 mV s^{-1}. Under identified conditions, the diffusion contributions of MCSe (**Fig. 3H**) and MCTe (**Fig. 3I**) are 19.8% and 65.7%, respectively. When the scan rate is varied from 1, 2, 3, 4, to 5 mV s^{-1}, the

diffusion contributions to total capacity of MCS (**Fig. 3J**) are 88.3%, 86.4%, 84.7.%, 83.2% and 81.7%, respectively. The diffusion contribution decreases with an increase in scan rate. However, at high scan rates, its diffusion contribution is still much higher than that of capacitive contribution, indicating that the redox reactions at high scan rates play a significant role in the electrocapacitive performance of MCS. In this case, it is mainly attributed to its unique texture that facilitates the diffusion of electrolytes. As for MCSe, an increase of the scan rate from 1 to 5 mV s^{-1} continuously enlarges the capacitive contribution. Its maximum contribution (88.7%) is seen at a scan rate of 5 mV s^{-1} (**Fig. 3K**). The results convincingly suggest a typical Faradaic capacitive performance of MCSe. In the case of MCTe (**Fig. 3L**), its capacitive contribution ratios are 24.4%, 29.9%, 34.3%, 38.2%, and 41.7% at the scan rates of 1, 2, 3, 4, and 5 mV s^{-1}, respectively. At the same scan rate, the diffusion contribution ratio of MCTe is lower than that of MCS as the diffusion-controlled ion intercalation at the electrodes is a relatively slow process. Meanwhile, low scan rates ensure sufficient times for ion migration and ion insertion, whereas at high scan rates, insufficient ion diffusion causes the oxidation-reduction reactions to predominate. The capacities of TMCs are thus mainly relied on the anions inside TMCs.

3.3. Performance of asymmetric supercapacitors

Based on above results obtained from three-electrode systems, a two-electrode device was ensembled to testify possibility of these TMC materials for practical energy storage applications. In this work, such a hybrid supercapacitor was constructed using MCS as the positive electrode material and hrGO as the negative electrode material. The hrGO electrode was further enhanced with 2,2,6,6-Tetramethylpiperidin-1-oxyl (TEMPO) dissolved in 2 M KOH. In this regard, the negative electrode is expected to have a high specific capacity and a wide redox potential range. For example, in the CVs of 10 mM TEMPO on the hrGO electrode at different scan rates (e.g., from 5 to 200 mV s^{-1}), there are reversible redox peaks at around -0.35 V (**Fig. S11A**). They waves are attributed to the transition from the aminooxy anion state to the nitroxide radical state [49]. With an increase of the scan rate, both the redox faradaic and non-faradaic currents increase, indicative of fast K^+ ions diffusion onto hrGO surfaces. The corresponding GCD curves of the hrGO + TEMPO system (**Fig. S11B**) deviated from nonlinear shapes, indicating electrochemical performance of such a system. The voltage plateaus at around -0.35 V correspond to the redox peaks at CVs. The specific capacity of this system was calculated based on its CVs and GCD curves. Its highest specific capacity is 361.2 C g^{-1}, obtained at a scan rate of 5 mV s^{-1}. It maintains 300.0 C g^{-1} when the scan rate is 200 mV s^{-1}, namely 83.1% retention of its initial capacity (**Fig. S11C**). Meanwhile, this system tends to have

higher specific capacity at lower current densities. For example, the specific capacity at a current density of 1 A g^{-1} is 483.0 C g^{-1}, 66.6% of that obtained at a current density of 20 A g^{-1} (**Fig. S11D**). Furthermore, the cycling stability of the hrGO + TEMPO system was tested with the GCD techniques at a current density of 15 A g^{-1}. Even after 4000 charge/discharge cycles, the hrGO + TEMPO system maintains 83.9% of its initial capacity (**Fig. S11E**). The R_{ct} values of this system are 0.3 Ω and 0.4 Ω before and after such a cycling test, respectively (**Fig. S11F**). The self-discharge and leakage current are also important parameters for redox-electrolytes in terms of practical applications. According to **Fig. S12**, after a rapid self-discharge decline in the first half hour, the output voltage of hrGO in KOH + TEMPO electrolyte is approximately 0.03 V after 10 hours, whereas it is -0.02 V in KOH electrolyte after ten hours. It is evident that hrGO maintains its low self-discharge characteristics even in redox electrolytes. The leakage current of hrGO rapidly stabilizes at 9.9 μA in KOH+TEMPO electrolytes compared with 2.5 μA in KOH electrolytes after 2 h for redox shuttling.

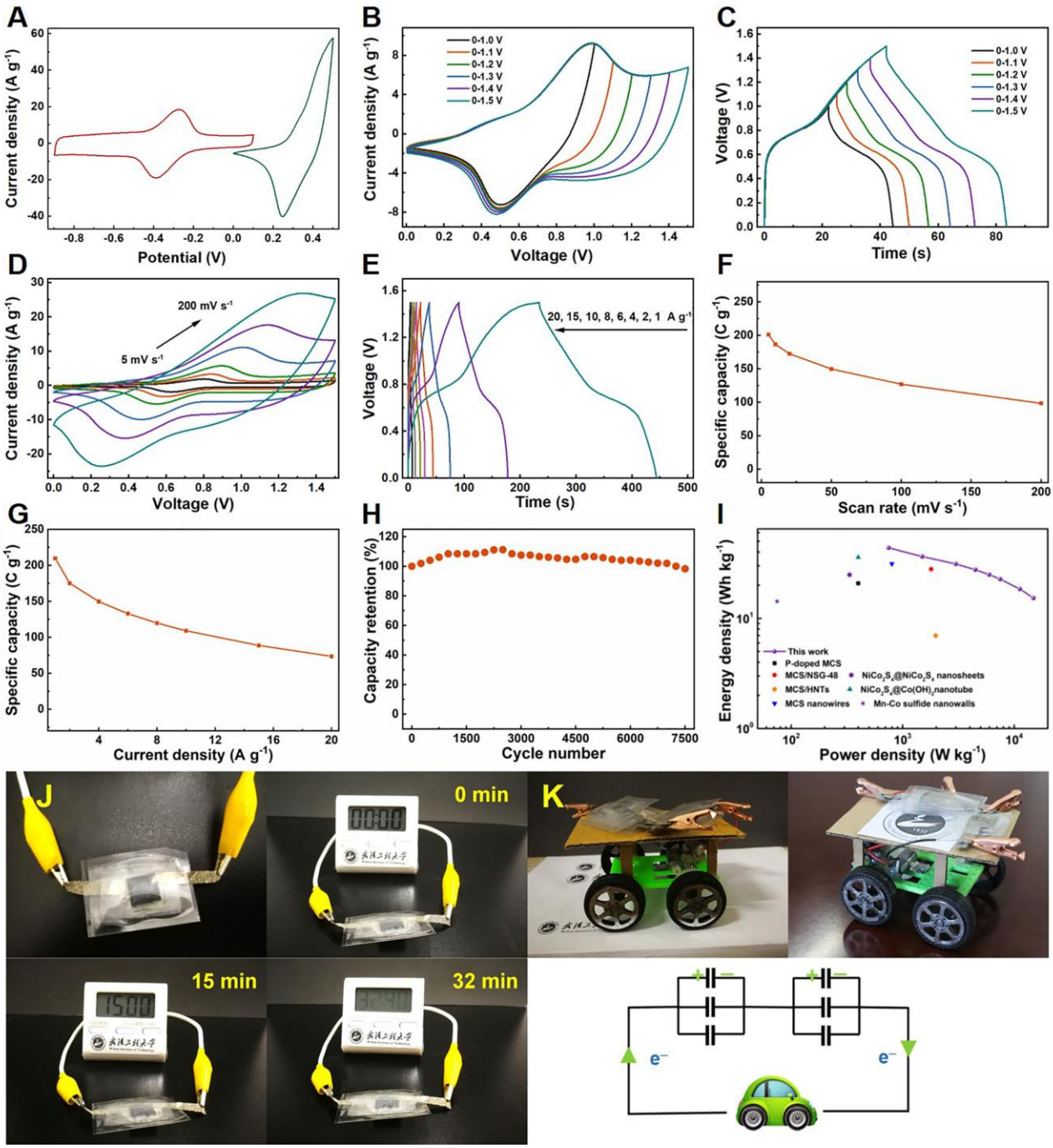

Fig. 4. Performance of an MCS || hrGO ASC device: (A) CVs of a hrGO electrode and a MCS electrode at a scan rate of 20 mV s^{-1}; (B) CVs at a scan rate of 50 mV s^{-1} with different cell voltages; (C) GCD curves at a current density of 4 A g^{-1} within various cell voltages; (D) CVs and (E) GCD curves at various scan rates and current densities; Calculated specific capacity as a function of scan rate (F) and current density (G); (H) the capacity retention over 7500 charge/discharge cycles at a current density of 10 A g^{-1}; (I) Comparison of the Ragone plots for different devices; (J) Photographs of operating an electronic timer; (K) Demonstration of driving a toy car.

Prior to the assemble of an asymmetric SC device, experimental conditions were optimized. For example, the charges stored by the positive and negative electrodes were firstly balanced. The mass ratio of the positive electrode (m_+) to the negative electrode (m_-) was fixed to 0.8 when the scan rate was set to 20 mV s^{-1}. Moreover, the voltage of the MCS (+) || hrGO(-) was optimized to be 1.5 V (**Fig. 4A**) after taking the voltage windows of the MCS (0 – 0.5 V) and the hrGO + TEMPO system (-0.9 – 0.1 V) into account.

The CV and GCD curves of this ASC device were then recorded within different voltage windows at a scan rate of 50 mV s^{-1} (**Fig. 4B**) and a current density of 4 A g^{-1} (**Fig. 4C**). Interestingly, no obvious oxygen evolution is observed even the voltage is higher than 1.5 V, an indication of well-balanced active masses on both electrodes. Since the CV within a voltage window of 1.5 V shows the largest area with distinct redox behaviour, the operation voltage of the ASC device was set to 1.5 V. The GCD curves of this ASC devices were also recorded at different voltage windows (e.g., ranging from 1.0 to 1.5 V). Similar results are obtained with those from the CVs.

The CVs of the ASC device (MCS || hrGO) were then collected at different scan rates (e.g., from 5 to 200 mV s^{-1}) and within a voltage window of 1.5 V (**Fig. 4D**). The change of scan rate does not lead to obvious variation of the shape of the CVs. An increase of the scan rate results in slowly enhanced current response, demonstrating a fast charge delivery rate of the ASC device. The calculated specific capacities are 201.0, 186.5, 172.4, 149.6, 126.9, and 98.4 C g^{-1} at the scan rates of 5, 10, 20, 50, 100, and 200 mV s^{-1}, respectively. The rate capability of 49.0% is maintained even at a scan rate of 200 mV s^{-1} (**Fig. 4F**). Meanwhile, the GCD curves of this ASC device (**Fig. 4E**) were recorded at different current densities (e.g., from 1 to 20 A g^{-1}). The charge curves are nearly symmetrical to their discharge counterparts, suggesting a high coulombic efficiency as well as well-matched mass balance between the positive and negative electrodes. Based on these GCD curves, the calculated capacities are 209.7, 175.1, 149.7, 132.9, 119.7, 109.1, 88.7 and 73.5 C g^{-1} at the current densities of 1, 2, 4, 6, 8, 10, 15, and 20 A g^{-1}, respectively. The rate performance is 35.1% even at the current density of 20 A g^{-1} (**Fig. 4G**). The cycling stability test of the ASC device was conducted when a current density of at 10 A g^{-1} was applied (**Fig. 4H**). This device exhibits remarkable cycling endurance. It retains 98.3% of the capacity retention after 7500 consecutive GCD cycles.

The energy densities and power densities, two key parameters to describe the practical usage of an ASC device were estimated. They are shown as a Ragone plot (**Fig. 4I**), where also compares with other SC devices. Our MCS || hrGO ASC device delivers a maximum specific energy of 43.7 Wh kg^{-1} at a specific power of 750.3 W kg^{-1}, or a maximum power density of 15.3 kW kg^{-1} at a specific energy density of 14898.6 W kg^{-1}. The highest energy density of our-assembled MCS || hrGO ASC device is superior to that of some recently reported SC devices, including P-MCS || AC [50], MCS |

NSG || NSG [51], MCS | HNTs || MCS | HNTs [52], MCS || rGO [53], $NiCo_2S_4$@$Co(OH)_2$ || AC [54], $NiCo_2S_4$ nanotube@$NiCo_2S_4$ nanosheet || rGO [55], and MCS | GNF || AC [56] devices. The potential usage of our MCS || hrGO ASC device was further verified through its exploration to operate an electronic timer (**Fig. 4J**). The electronic timer ran for more than 32 min only by one ASC device. Three connected ASC devices in series and then two groups in parallel drove a homemade toy car (**Fig. 4K**). Such fully charged device drove the toy car for about 11.4 m. Therefore, our MCS || hrGO ASC device has the potential for practical applications.

4. Conclusion

In summary, the effect of anions on the electrochemical performance of nanoneedle-like and bimetallic (Mn–Co) chalcogenides has been clarified. Originating from their different geometric features and redox activities in alkaline solutions, the S-anion based chalcogenide exhibits higher and more stable capacity than the Se- and Te-based chalcogenides. The constructed asymmetric supercapacitor device using S-anion based chalcogenide and holey graphene feature excellent rate capability, long cycling life, and high power densities as well as high energy densities. Such devices have been proved to be promising for different practical applications. This study is of great importance to design and synthesize proper and useful bimetallic chalcogenides for energy storage applications.

Acknowledgements

This work was financially supported by the Natural Science Foundation of Hubei Province, China (No.2021CFB1192), the Graduate Innovative Fund of Wuhan Institute of Technology of China, Youths Science Foundation of Wuhan Institute of Technology (No.19QD36), and the Opening fund of Hubei Key Laboratory of Bioinorganic Chemistry & Materia Medica (No. BCMM202105).

Conflict of Interest

The authors declare no conflict of interest.

References

[1] N. Abas, A. Kalair, N. Khan, Review of fossil fuels and future energy technologies, Futures 69 (2015) 31-49.

[2] R. Kothari, V.V. Tyagi, A. Pathak, Waste-to-energy: a way from renewable energy sources to sustainable development, Renew. Sust. Energ. Rev. 14 (2010) 3164-3170.

[3] V. Khare, S. Nema, P. Baredar, Solar–wind hybrid renewable energy system: a review, Renew. Sust. Energ. Rev. 58 (2016) 23-33.

[4] A. Razmjoo, L. Gakenia Kaigutha, M.A. Vaziri Rad, M. Marzband, A. Davarpanah, M. Denai, A technical analysis investigating energy sustainability utilizing reliable renewable energy sources to reduce CO_2 emissions in a high potential area, Renew. Energ. 164 (2021) 46-57.

[5] Y. Shao, M.F. El-Kady, J. Sun, Y. Li, Q. Zhang, M. Zhu, H. Wang, B. Dunn, R.B. Kaner, Design and mechanisms of asymmetric supercapacitors, Chem. Rev. 118 (2018) 9233-9280.

[6] Y. Yao, H. Li, Y. Yu, C. Du, L. Wan, H. Ye, J. Chen, Y. Zhang, M. Xie, Stabilizing microstructure of Co-Ni layered double hydroxides by magnesium doping and confinement in carbonaceous mesopores for ultrahighly-stable asymmetric supercapacitor, J. Energy Storage 59 (2023), 106422.

[7] Y. Yao, Y. Yu, L. Wan, C. Du, Y. Zhang, J. Chen, M. Xie, Structurally-stable Mg-Co-Ni LDH grown on reduced graphene by ball-milling and ion-exchange for highly-stable asymmetric supercapacitor, J. Colloid Interf. Sci. 649 (2023) 519-527.

[8] M. Xie, S. Duan, Y. Shen, K. Fang, Y. Wang, M. Lin, X. Guo, In-situ-grown $Mg(OH)_2$-derived hybrid α-$Ni(OH)_2$ for highly stable supercapacitor, ACS Energy Lett. 1 (2016) 814-819.

[9] A. Afif, S.M.H. Rahman, A. Tasfiah Azad, J. Zaini, M.A. Islan, A.K. Azad, Advanced materials and technologies for hybrid supercapacitors for energy storage – A review, J. Energy Storage 25 (2019), 100852.

[10] Y. Zhang, L. Zhang, T.a. Lv, P.K. Chu, K. Huo, Two-dimensional transition metal chalcogenides for alkali metal ions storage, ChemSusChem 13 (2020) 1114-1154.

[11] J. Feng, X. Li, Z. Shi, C. Zheng, X. Li, D. Leng, Y. Wang, J. Liu, L. Zhu, 2D ductile transition metal chalcogenides (TMCs): novel high-performance Ag_2S nanosheets for ultrafast photonics, Adv. Opt. Mater. 8 (2020), 1901762.

[12] K.C. Majhi, M. Yadav, Transition metal chalcogenides based nanocomposites as efficient electrocatalyst for hydrogen evolution reaction over the entire pH range, Int. J. Hydrogen Energ. 45 (2020) 24219-24231.

[13] H. Fan, P. Mao, H. Sun, Y. Wang, S.S. Mofarah, P. Koshy, H. Arandiyan, Z. Wang, Y. Liu, Z. Shao, Recent advances of metal telluride anodes for high-performance lithium/sodium–ion batteries, Mater. Horiz. 9 (2022) 524-546.

[14] W. Liu, H. Niu, J. Yang, K. Cheng, K. Ye, K. Zhu, G. Wang, D. Cao, J. Yan, Ternary transition metal sulfides embedded in graphene nanosheets as both the anode and cathode for high-performance asymmetric supercapacitors, Chem. Mater. 30 (2018) 1055-1068.

[15] S. Sambasivam, C.V.V.M. Gopi, H.M. Arbi, Y.A. Kumar, H.-J. Kim, S.A. Zahmi, I.M. Obaidat, Binder-free hierarchical core-shell-like $CoMn_2O_4$@MnS nanowire arrays on nickel foam as a battery-type electrode material for high-performance supercapacitors, J. Energy Storage 36 (2021), 102377.

[16] S. Nandhini, G. Muralidharan, Graphene encapsulated NiS/Ni_3S_4 mesoporous nanostructure: a superlative high energy supercapacitor device with excellent cycling performance, Electrochim. Acta 365 (2021), 137367.

[17] S. Subhadarshini, E. Pavitra, G.S. Rama Raju, N.R. Chodankar, A. Mandal, S. Roy, S. Mandal, M.V.B. Rao, D.K. Goswami, Y.S. Huh, N.C. Das, One-pot facile synthesis and electrochemical evaluation of selenium enriched cobalt selenide nanotube for supercapacitor application, Ceram. Int. 47 (2021) 15293-15306.

[18] E.-K. Kim, H.T. Bui, N.K. Shrestha, C.Y. Shin, S.A. Patil, S. Khadtare, C. Bathula, Y.-Y. Noh, S.-H. Han, An enhanced electrochemical energy conversion behavior of thermally treated thin film of 1-dimensional CoTe synthesized from aqueous solution at room temperature, Electrochim. Acta 260 (2018) 365-371.

[19] J. Sun, C. Xu, H. Chen, A review on the synthesis of $CuCo_2O_4$-based electrode materials and their applications in supercapacitors, J. Materiomics 7 (2021) 98-126.

[20] R. Wu, J. Sun, C. Xu, H. Chen, $MgCo_2O_4$-based electrode materials for electrochemical energy storage and conversion: a comprehensive review, Sustain. Energ. Fuels 5 (2021) 4807-4829.

[21] Y. Liu, X. Du, Y. Li, E. Bao, X. Ren, H. Chen, X.D Tian, C.J. Xu, Nanosheet-assembled porous $MnCo_2O_{4.5}$ microflowers as electrode material for hybrid supercapacitors and lithium-ion batteries, J. Colloid Interf. Sci. 627 (2022) 815-826.

[22] X. Du, X. Ren, C. Xu, H. Chen, Recent advances on the manganese cobalt oxides as electrode materials for supercapacitor applications: a comprehensive review, J. Energy Storage 68 (2023), 107672.

[23] S.M.N. Jeghan, G. Lee, One-dimensional hierarchical nanostructures of $NiCo_2O_4$, $NiCo_2S_4$ and $NiCo_2Se_4$ with superior electrocatalytic activities toward efficient oxygen evolution reaction, Nanotechnology 31 (2020), 295405.

[24] X. Zhou, Z. Jia, X. Zhang, B. Wang, X. Liu, B. Xu, L. Bi, G. Wu, Electromagnetic wave absorption performance of $NiCo_2X_4$ (X = O, S, Se, Te) spinel structures, Chem. Eng. J. 420 (2021), 129907.

[25] H. Xuan, Y. Guan, X. Han, X. Liang, Z. Xie, P. Han, Y. Wu, Hierarchical MC-LDH/rGO@$NiCo_2S_4$ heterostructures on Ni foam with enhanced electrochemical properties for battery-supercapacitors, Electrochim. Acta 335 (2020), 135691.

[26] E. Bao, X. Ren, R. Wu, X. Liu, H. Chen, Y. Li, C. Xu, Porous $MgCo_2O_4$ nanoflakes serve as electrode materials for hybrid supercapacitors with excellent performance, J. Colloid Interf. Sci. 625 (2022) 925-935.

[27] S. He, F. Guo, Q. Yang, H. Mi, J. Li, N. Yang, J. Qiu, Design and fabrication of hierarchical NiCoP–MOF heterostructure with enhanced pseudocapacitive properties, Small 17 (2021), 2100353.

[28] A.D. Jagadale, G. Guan, X. Li, X. Du, X. Ma, X. Hao, A. Abudula, Ultrathin nanoflakes of cobalt–manganese layered double hydroxide with high reversibility for asymmetric supercapacitor, J. Power Sources 306 (2016) 526-534.

[29] X. Hu, X. Tian, Y.-W. Lin, Z. Wang, Nickel foam and stainless steel mesh as electrocatalysts for hydrogen evolution reaction, oxygen evolution reaction and overall water splitting in alkaline media, RSC Adv. 9 (2019) 31563-31571.

[30] Q. Zhang, Q. Shi, Y. Yang, Q. Zang, Z. Xiao, X. Zhang, L. Wang, 2D nanosheet/3D cubic framework Ni–Co sulfides for improved supercapacitor performance via structural engineering, Dalton Trans. 49 (2020) 8162-8168.

[31] B. Liu, D. Kong, J. Zhang, Y. Wang, T. Chen, C. Cheng, H.Y. Yang, 3D hierarchical Co_3O_4@Co_3S_4 nanoarrays as cathode materials for asymmetric pseudocapacitors, J. Mater. Chem. A 4 (2016) 3287-3296.

[32] L. Wang, Z. Feng, H. Zhang, D. Li, P. Xing, One-step electrodeposited 3D porous $NiCoSe_2$ nanosheet array for high-performance asymmetric supercapacitors, Nanotechnology 31 (2020), 125403.

[33] L. Cui, H. Qi, N. Wang, X. Gao, C. Song, J. Yang, G. Wang, S. Kang, X. Chen, N/S co-doped CoSe/C nanocubes as anode materials for Li-ion batteries, Nanotechnol. Rev. 11 (2022) 244-251.

[34] M. Manikandan, K. Subramani, M. Sathish, S. Dhanuskodi, Hydrothermal synthesis of cobalt telluride nanorods for a high performance hybrid asymmetric supercapacitor, RSC Adv. 10 (2020) 13632-13641.

[35] C. Hu, J. Chen, Y. Wang, Y. Huang, S. Wang, A telluride-doped porous carbon as highly efficient bifunctional catalyst for rechargeable Zn-air batteries, Electrochim. Acta 404 (2022), 139606.

[36] Y.V. Lim, S.Z. Huang, Q.Y. Wu, D.Z. Kong, Y. Wang, Y.F. Zhu, Y.X. Wang, Y.X. Wang, H.K. Liu, S.X. Dou, L.K. Ang, H.Y. Yang, Super-kinetically pseudocapacitive $MnCo_2S_4$ nanourchins toward high-rate and highly stable sodium-ion storage, Adv. Funct. Mater. 30 (2020), 1909702.

[37] M.L. Aparna, T. Thomas, G.R. Rao, Battery-like supercapacitive behavior of urchin-shaped $NiCo_2O_4$ and comparison with $NiCo_2X_4$ (X = S, Se, Te), J. Electrochem. Soc. 169 (2022), 020515.

[38] S. Liu, D. Ni, H.-F. Li, K.N. Hui, C.-Y. Ouyang, S.C. Jun, Effect of cation substitution on the pseudocapacitive performance of spinel cobaltite MCo_2O_4 (M = Mn, Ni, Cu, and Co), J. Mater. Chem. A 6 (2018) 10674-10685.

[39] L. Abbasi, M. Arvand, S.E. Moosavifard, Facile template-free synthesis of 3D hierarchical ravine-like interconnected MCS nanosheet arrays for hybrid energy storage device, Carbon 161 (2020) 299-308.

[40] Z. Liu, Y. Qiu, A. Zhang, W. Yang, C.J. Barrow, J.M. Razal, J. Liu, In situ embedding of cobalt sulfide quantum dots among transition metal layered double hydroxides for high performance all-solid-state asymmetric supercapacitors, J. Mater. Chem. A 9 (2021) 22573-22584.

[41] J. Zhou, Y. Dou, T. He, A. Zhou, X.-J. Kong, X.-Q. Wu, T. Liu, J.-R. Li, Revealing the effect of anion-tuning in bimetallic chalcogenides on electrocatalytic overall water splitting, Nano Research 14 (2021) 4548-4555.

[42] L. Tao, M. Huang, S. Guo, Q. Wang, M. Li, X. Xiao, G. Cao, Y. Shao, Y. Shen, Y. Fu, M. Wang, Surface modification of $NiCo_2Te_4$ nanoclusters: a highly efficient electrocatalyst for overall water-splitting in neutral solution, Appl. Catal. B 254 (2019) 424-431.

[43] B. Ye, C. Gong, M. Huang, Y. Tu, X. Zheng, L. Fan, J. Lin, J. Wu, Improved performance of a CoTe//AC asymmetric supercapacitor using a redox additive aqueous electrolyte, RSC Adv. 8 (2018) 7997-8006.

[44] X. Wang, L. Xu, K. Song, R. Yang, L. Jia, X. Guo, X. Jing, J. Wang, Synthesis of $MnCo_2O_4$@MCS core/shell micro-nanostructures on Ni foam for high performance asymmetric supercapacitors, Colloids Surf. A Physicochem. Eng. Asp. 570 (2019) 73-80.

[45] Y. Xue, X. Guo, M. Wu, J. Chen, M. Duan, J. Shi, J. Zhang, F. Cao, Y. Liu, Q. Kong, Zephyranthes-like Co_2NiSe_4 arrays grown on 3D porous carbon frame-work as electrodes for advanced supercapacitors and sodium-ion batteries, Nano Research 14 (2021) 3598-3607.

[46] Q. Wang, Y. Ma, Y. Wu, D. Zhang, M. Miao, Flexible asymmetric threadlike supercapacitors based on $NiCo_2Se_4$ nanosheet and $NiCo_2O_4$/polypyrrole electrodes, ChemSusChem 10 (2017) 1427-1435.

[47] J.L. Liu, J. Wang, C.H. Xu, H. Jiang, C.Z. Li, L.L. Zhang, J.Y. Lin, Z.X. Shen, Advanced energy storage devices: basic principles, analytical methods, and rational materials design, Adv. Sci. 5 (2018), 1700322.

[48] J. Wang, J. Polleux, J. Lim, B. Dunn, Pseudocapacitive contributions to electrochemical energy storage in TiO_2 (anatase) nanoparticles, J. Phys. Chem. C 111 (2007) 14925-14931.

[49] G.A.M. Ali, E. Megiel, J. Romański, H. Algarni, K.F. Chong, A wide potential window symmetric supercapacitor by TEMPO functionalized MWCNTs, J. Mol. Liq. 271 (2018) 31-39.

[50] H. Jia, Y. Song, J. Wu, W. Fu, J. Zhao, X. Liu, A novel P-doped MCS nanoneedles assembled dandelion-like structure for high performance hybrid supercapacitors, Mater. Lett. 233 (2018) 55-58.

[51] H. Wang, K. Zhang, Y. Song, J. Qiu, J. Wu, L. Yan, MCS nanoparticles anchored to N- and S-codoped 3D graphene as a prominent electrode for asymmetric supercapacitors, Carbon 146 (2019) 420-429.

[52] S.K. Shinde, G.S. Ghodake, N.C. Maile, H.M. Yadav, A.D. Jagadale, M.B. Jalak, A.A. Kadam, S. Ramesh, C. Bathula, D.Y. Kim, Designing of nanoflakes anchored nanotubes-like MCS/halloysite composites for advanced battery like supercapacitor application, Electrochim. Acta 341 (2020), 135973.

[53] S. Liu, S.C. Jun, Hierarchical manganese cobalt sulfide core–shell nanostructures for high-performance asymmetric supercapacitors, J. Power Sources 342 (2017) 629-637.

[54] R. Li, S. Wang, Z. Huang, F. Lu, T. He, $NiCo_2S_4$@$Co(OH)_2$ core-shell nanotube arrays in situ grown on Ni foam for high performances asymmetric supercapacitors, J. Power Sources 312 (2016) 156-164.

[55] H. Chen, S. Chen, H. Shao, C. Li, M. Fan, D. Chen, G. Tian, K. Shu, Hierarchical $NiCo_2S_4$ nanotube@ $NiCo_2S_4$ nanosheet arrays on Ni foam for high-performance supercapacitors, Chemistry – An Asian Journal 11 (2016) 248-255.

[56] M. Yu, X. Li, Y. Ma, R. Liu, J. Liu, S. Li, Nanohoneycomb-like manganese cobalt sulfide/three dimensional graphene-nickel foam hybid electrodes for high-rate capability supercapacitors, Appl. Surf. Sci. 396 (2017) 1816-1824.

Supporting Information

Role of anion on the electrochemical performance of MnCo chalcogenides

Ying Zhang [a], Weikang He [a], Jingjing Li [a], Yuanyuan Zhang [a], Juan Yang [a], Ting Zeng [a, *], Nianjun Yang [b]

[a] School of Chemistry and Environmental Engineering, Key Laboratory of Green Chemical Engineering Process of Ministry of Education, Hubei Key Laboratory of Novel Reactor and Green Chemical Technology, Wuhan Institute of Technology, Wuhan 430073, China

[b] Department of Chemistry, Hasselt University, Agoralaan 1 - Buidling D, 3590 Diepenbeek, Belgium

Corresponding authors.

E-mail address: tingzeng1201@wit.edu.cn (Ting Zeng)

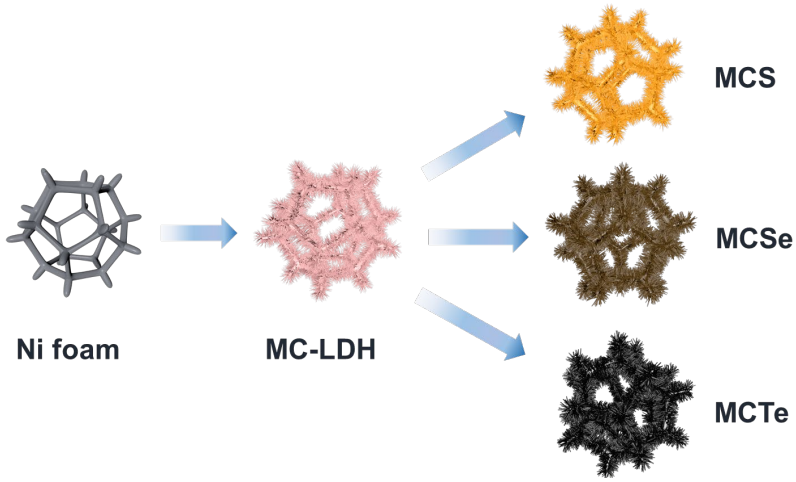

Fig. S1. Schematic illustration of the synthesis of MCX (X = S, Se, Te) on the Ni foam.

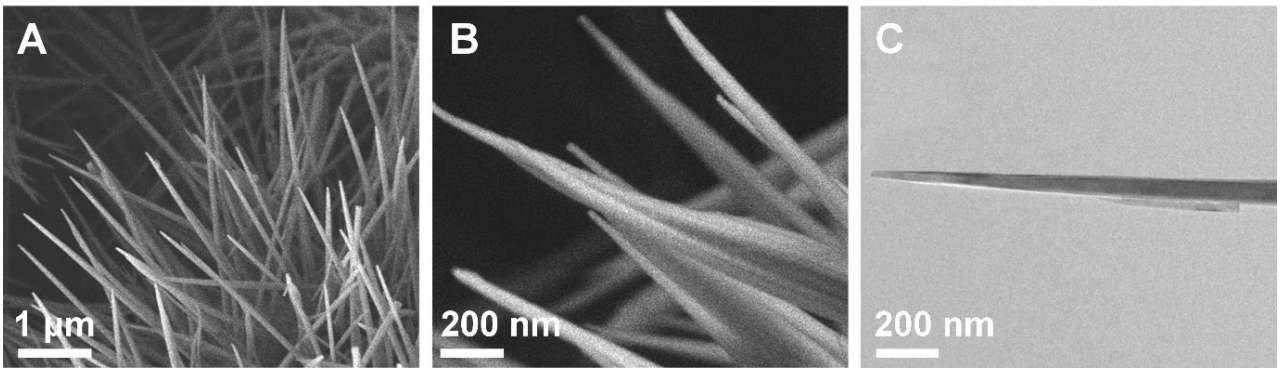

Fig. S2. (A, B) SEM and (C) TEM images of the MC-LDH precursor at low (A) and high (B) magnifications.

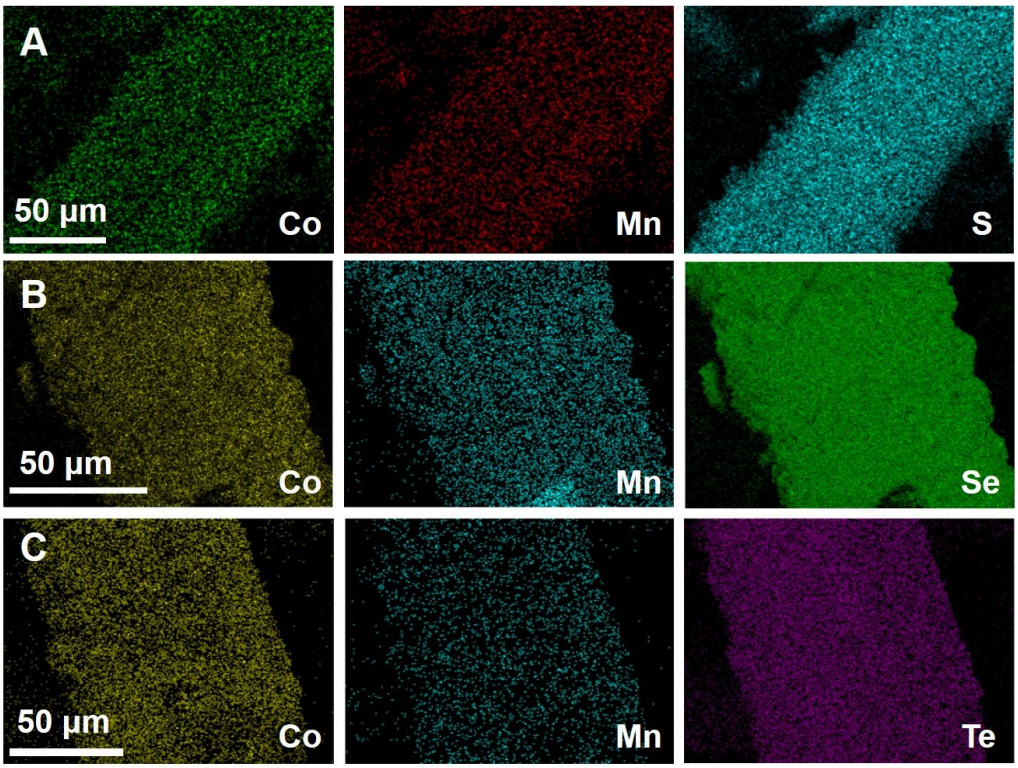

Fig. S3. The element mapping images of (A) MCS, (B) MCSe, and (C) MCTe.

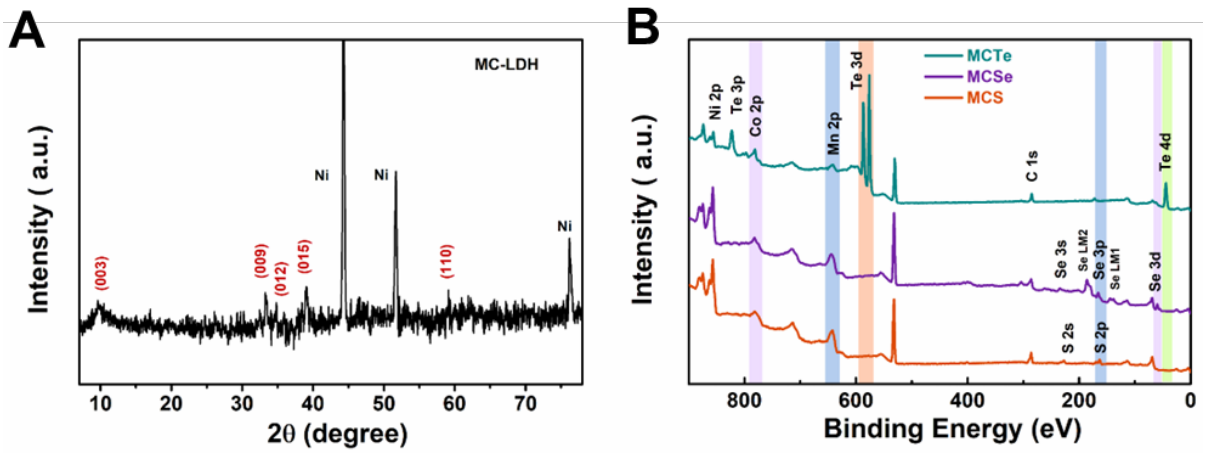

Fig. S4 (A)XRD patterns of the MnCo precursor; (B) XPS survey spectra of MCS, MCSe, and MCTe.

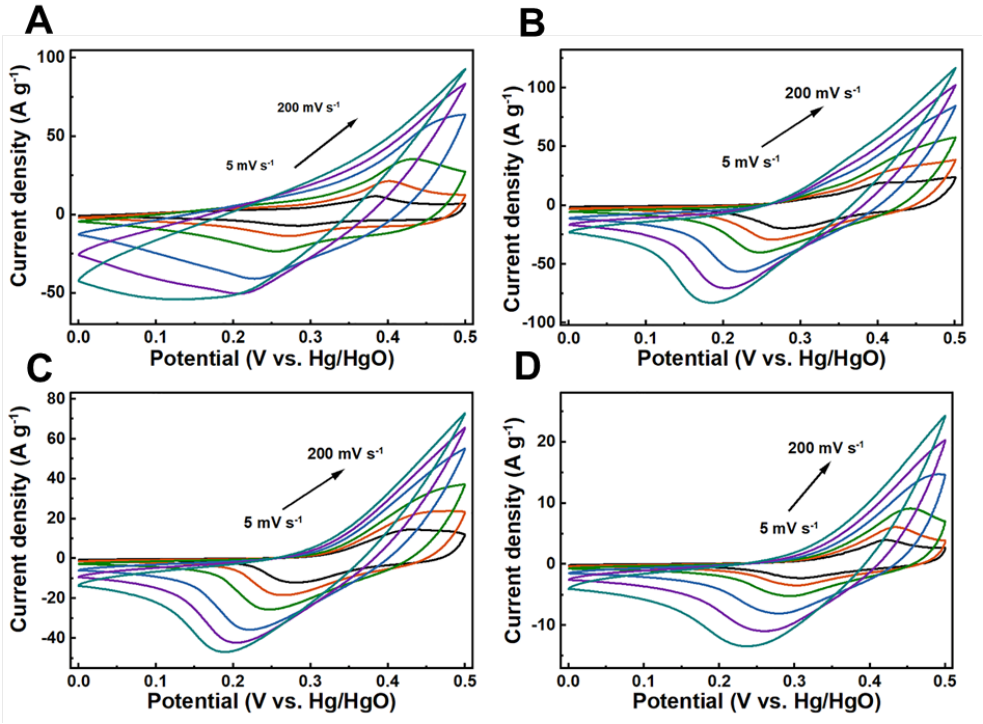

Fig. S5. CVs of (A) MC-LDH, (B) MCS, (C) MCSe, and (D) MCTe in 6 M KOH aqueous solution at different scan rates.

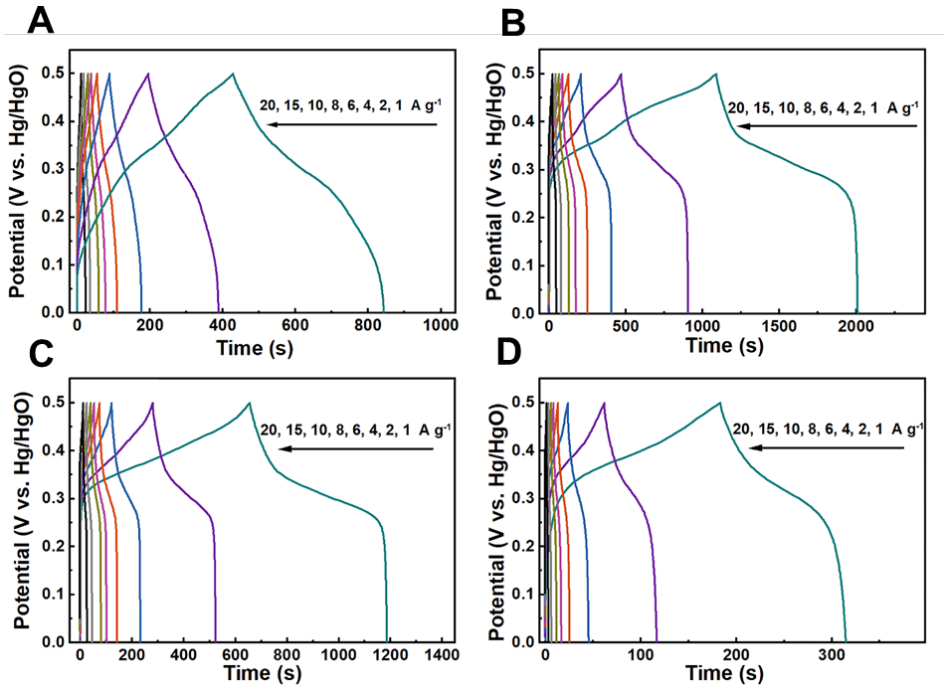

Fig. S6. GCD curves of (A) MC-LDH, (B) MCS, (C) MCSe, and (D) MCTe in 6 M KOH aqueous solution at different current densities.

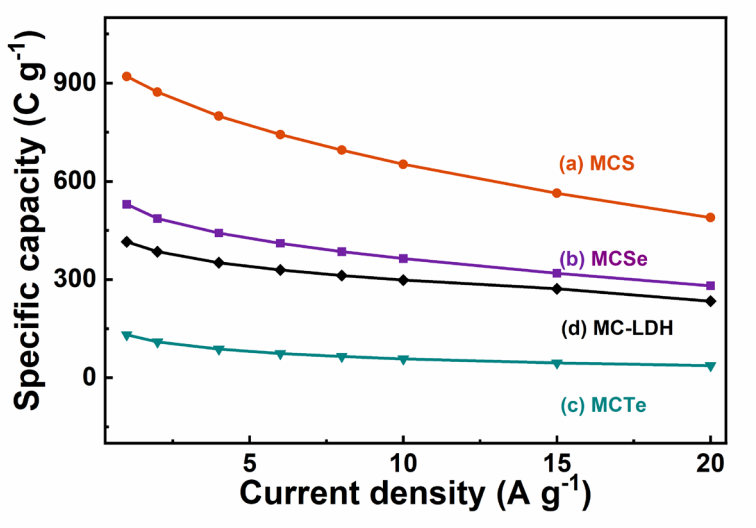

Fig. S7. Variation of specific capacities with the current densities for the MC-LDH, MCS, MnCSe, and MCTe.

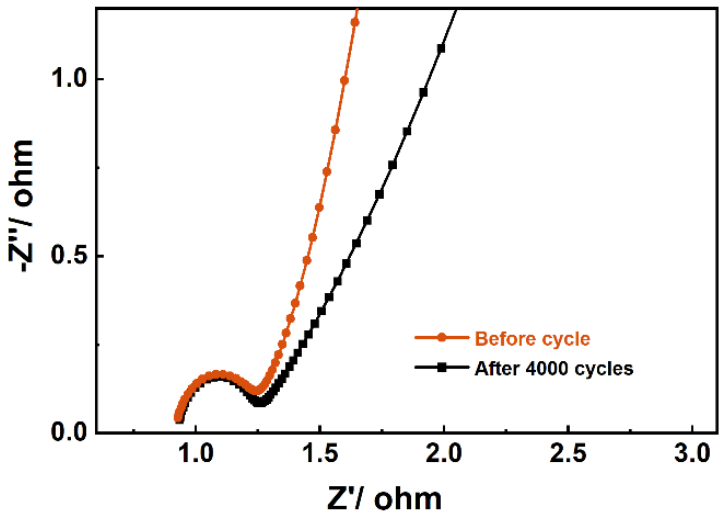

Fig. S8. Nyquist plots of the MCS electrodes recorded before and after 4000 charge/discharge cycles at a current density of 10 Ag^{-1}.

Table S1. Comparison of electrochemical performance of MCS-based electrodes reported in the literature.

Electrode	Electrolyte	Capacity	Rate capability	Capacity retention	Ref.
MCS /NSG-48	1 M KOH	1324.3 F g^{-1} (1 A g^{-1})	63.1% (1 to 32 A g^{-1})	90.9% (5000 cycles)	[1]
MCS nanotubes	3 M KOH	705.2 F g^{-1} (0.5 A g^{-1})	48.1% (0.5 to 10 A g^{-1})	92.6% (5000 cycles)	[2]
MCS needle	2 M KOH	1402 F g^{-1} (1 A g^{-1})	-	95.0%[c] (5000 cycles)	[3]
MCS/HNTs	1 M KOH	302 mA h g^{-1} (2 mA cm^{-2})	72.8% (2 to 7 mA cm^{-2})	-	[4]
MCS /$CoS_{1.097}$	3 M KOH	1006 F g^{-1} (1 A g^{-1})	70.5% (1 to 15 A g^{-1})	91.3%[c] (5000 cycles)	[5]
MCS @Ni-Co-S	3 M KOH	10.14 F cm^{-2} (1 mA cm^{-2})	82.3% (1 to 20 mA cm^{-2})	62.7% (5000 cycles)	[6]
MCS /Co_9S_8	6 M KOH	1100.5 F g^{-1} (1 A g^{-1})	59.8% (1 to 10 A g^{-1})	–	[7]
honeycomb-like MCS	3 M KOH	129.7 mA h g^{-1} (1 A g^{-1})	88.5% (1 to 10 A g^{-1})	87.8%[a] (4000 cycles)	[8]
P- MCS	6 M KOH	543.3 F g^{-1} (1 A g^{-1})	84.6% (1 to 10 A g^{-1})	–	[9]
MCS	6 M KOH	920.5 C g^{-1} (1 A g^{-1})	53.2% (1 to 20 A g^{-1})	87.9% (4000 cycles)	This work

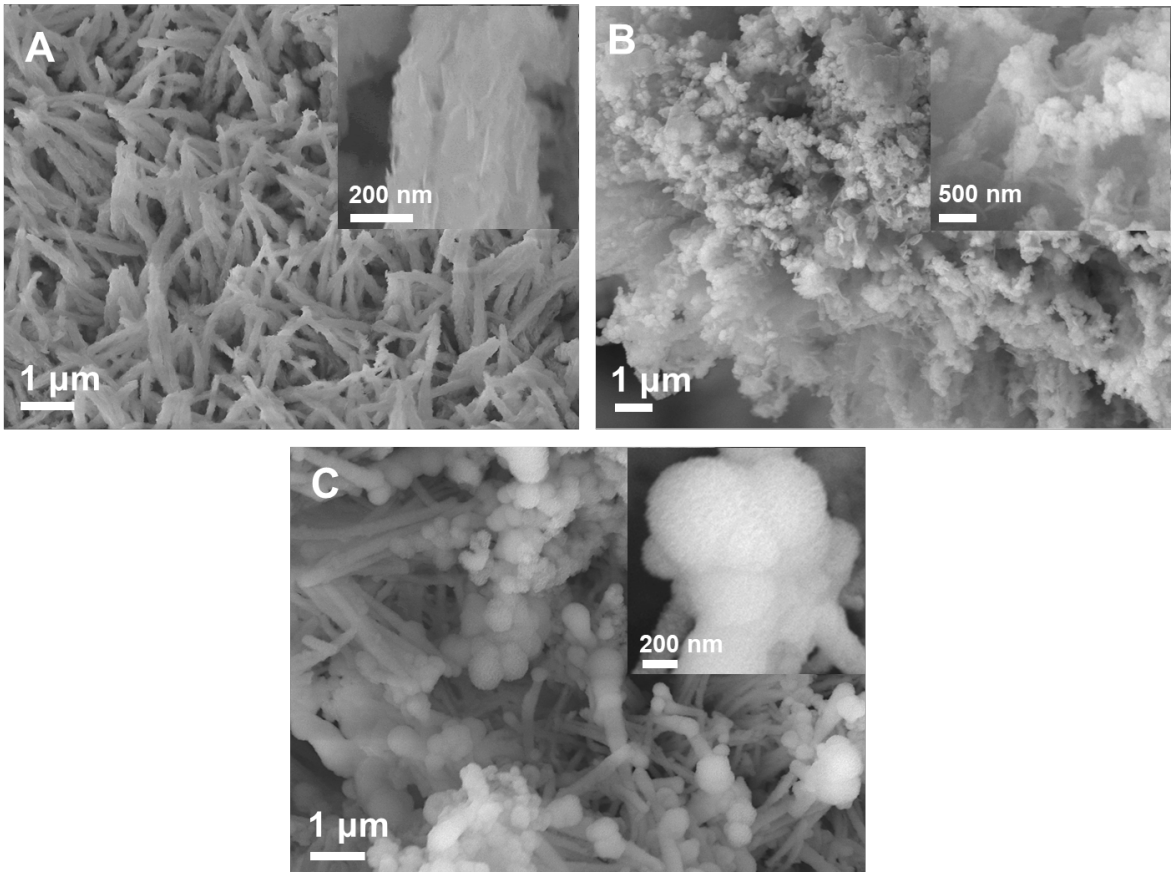

Fig. S9. The SEM images of (A) MCS, (B) MCSe, and (C) MCTe after 4000 charge/discharge cycles.

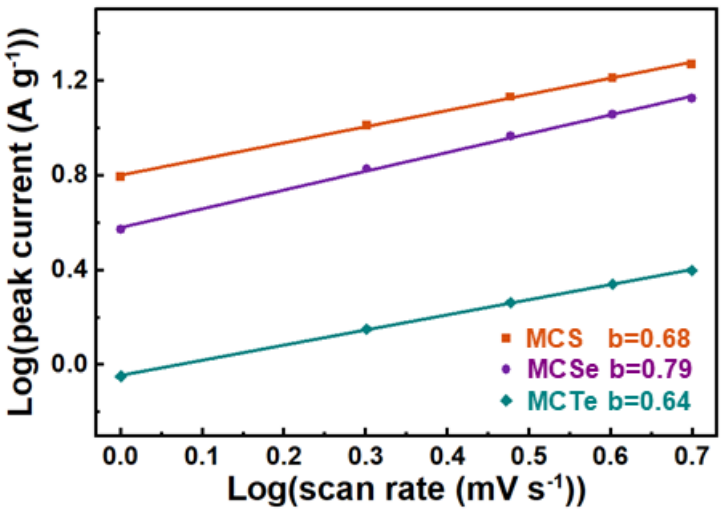

Fig. S10. Linear relationship between the logarithm values of peak current (log I_p) and those of scan rate (log v) on MCS, MCSe, and MCTe.

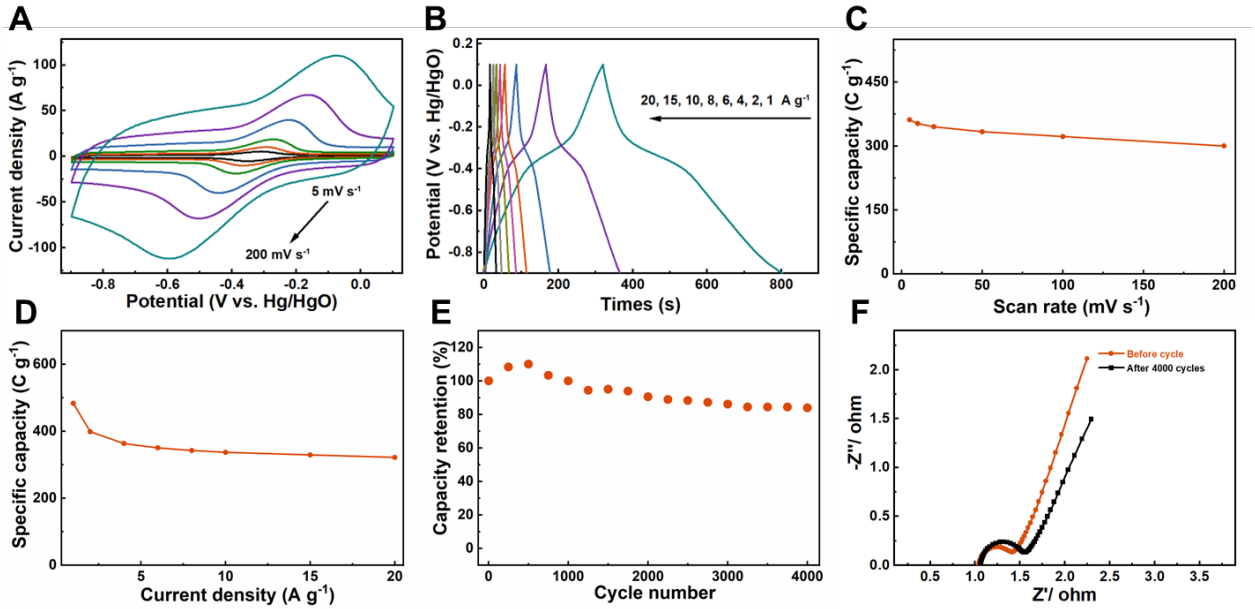

Fig. S11. Electrochemical performances of hrGO in the electrolyte of 2 M KOH + 10 mM TEMPO: (A) CVs at different scan rates, (B) GCD curves at different current densities; Specific capacities of hrGO in the electrolyte of 2 M KOH + 10 mM TEMPO at various scan rates (C) and current densities (D), (E) the capacity retention of a hrGO electrode over 4000 charge/discharge cycles at a current density of 10 A g^{-1}, (F) the Nyquist plots of hrGO obtained before and after 4000 charge/discharge cycles.

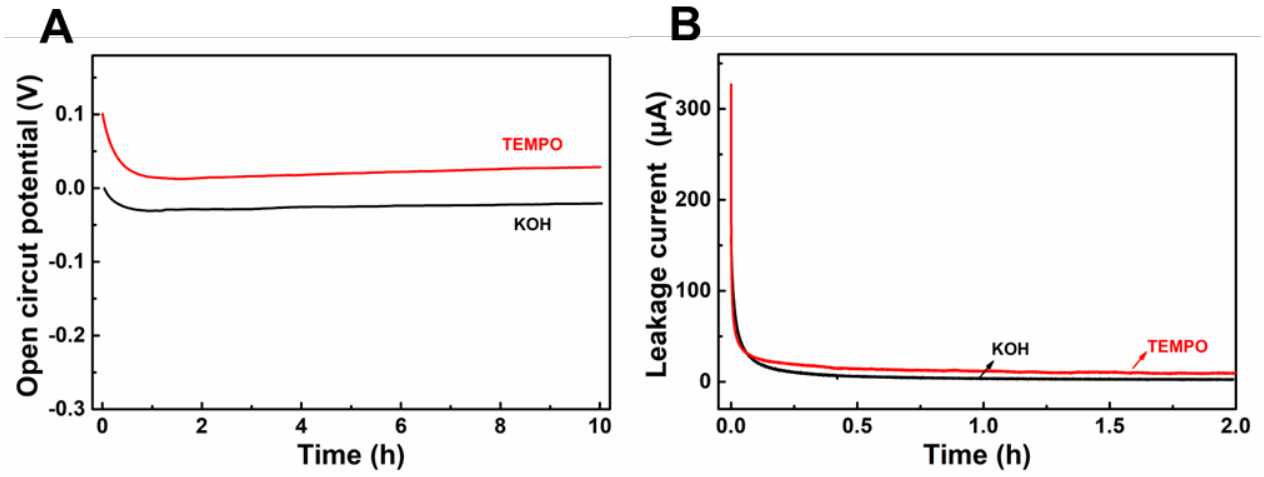

Fig. S12. (A) Self-discharge and (B) the leakage current of hrGO in the electrolyte of 2 M KOH + 10 mM TEMPO.

References

[1] H. Wang, K. Zhang, Y. Song, J. Qiu, J. Wu, L. Yan, $MnCo_2S_4$ nanoparticles anchored to N- and S-codoped 3D graphene as a prominent electrode for asymmetric supercapacitors, Carbon 146 (2019) 420-429.

[2] C.Z. Wie, Y.T. Sun, N.N. Zhan, M.Y. Liu, L.Y. Zhao, C. Cheng, D.J. Zhang, Preparation of hierarchical $MnCo_2S_4$ nanotubes for high-performance supercapacitors and non-enzymatic glucose sensors, Chemistryselect 2 (2017) 11154-11159.

[3] A.M. Elshahawy, X. Li, H. Zhang, Y.T. Hu, K.H. Ho, C. Guan, J. Wang, Controllable $MnCo_2S_4$ nanostructures for high performance hybrid supercapacitors, J. Mater. Chem. A 5 (2017) 7494-7506.

[4] S.K. Shinde, G.S. Ghodake, N.C. Maile, H.M. Yadav, A.D. Jagadale, M.B. Jalak, A.A. Kadam, S. Ramesh, C. Bathula, D.Y. Kim, Designing of nanoflakes anchored nanotubes-like $MnCo_2S_4$/halloysite composites for advanced battery like supercapacitor application, Electrochim. Acta 341 (2020), 135973.

[5] X. Yu, J.L. Yu, L. Hou, A. Gagnoud, Y. Fautrelle, Z.M. Ren, X. Li, Double-shelled hollow hetero-$MnCo_2S_4$/$CoS_{1.097}$ spheres with carbon coating for advanced supercapacitors, J. Energy Storage 408 (2018) 65-73.

[6] K. Yu, W.M. Tang, J. Dai, Double-layer $MnCo_2S_4$@Ni-Co-S core/shell nanostructure on nickel foam for high-performance supercapacitor, Phys. Status Solidi A 215 (2018), 1800147.

[7] H. Jia, J. Wang, W. Fu, J. Hu, Y. Liu, In-situ MOFs-derived hollow Co_9S_8 polyhedron welding on the top of $MnCo_2S_4$ nanoneedles for high performance hybrid supercapacitors, Chem. Eng. J. 391 (2020), 123541.

[8] K.V.G. Raghavendra, C.V.V.M. Gopi, R. Vinodh, S.S. Rao, I.M. Obaidat, H.-J. Kim, Facile synthesis of nanoparticles anchored on honeycomb-like $MnCo_2S_4$ nanostructures as a binder-free electroactive material for supercapacitors, J. Energy Storage 27 (2020), 101159.

[9] H. Jia, Y. Song, J. Wu, W. Fu, J. Zhao, X. Liu, A novel P-doped $MnCo_2S_4$ nanoneedles assembled dandelion-like structure for high performance hybrid supercapacitors, Mater. Lett. 233 (2018) 55–58.